Chiral excitonic organic photodiodes for direct detection of circular polarized light

ADVANCED FUNCTIONAL MATERIALS
www.afm-journal.de

Chiral Excitonic Organic Photodiodes for Direct Detection of Circular Polarized Light

*Matthias Schulz, Frank Balzer, Dorothea Scheunemann, Oriol Arteaga, Arne Lützen, Stefan C. J. Meskers, and Manuela Schiek**

A facile route to soft matter self-powered bulk heterojunction photodiode detectors sensitive to the circular polarization state of light is shown based on the intrinsic excitonic circular dichroism of the photoactive layer blend. As light detecting materials, enantiopure semiconducting small molecular squaraine derivates of opposite handedness are employed. Via Mueller matrix ellipsometry, the circular dichroism is proven to be of H-type excitonic nature and not originating from mesoscopic structural ordering. Within the green spectral range, the photodiodes convert circular polarized light into a handedness-dependent photocurrent with a maximum dissymmetry factor of ±0.1 corresponding to 5% overall efficiency for the polarization discrimination under short circuit conditions. On the basis of transfer matrix optical simulations, it is rationalized that the optical dissymmetry fully translates into a photocurrent dissymmetry for ease of device design. Thereby, the photodiode's ability to efficiently distinguish between left and right circularly polarized light without the use of external optical elements and voltage bias is demonstrated. This allows a straightforward and sustainable future design of flexible, lightweight, and compact integrated platforms for chiroptical imaging and sensing.

1. Introduction

The circular polarization of electromagnetic radiation is used routinely for data transmission in, e.g., satellite communication[1] and 3D cinematography.[2] Here, left (L) and right (R) handed circular polarized light (CPL) can be used as two independent channels to transmit information, doubling the rate of data transport compared to unpolarized light. Furthermore, source and receiver are decoupled and can rotate freely with respect to each other, while linearly polarized light would require azimuthal alignment. Yet successful employment of CPL based communication requires the availability of high fidelity CPL selective detectors. They may be realized by combining polarization manipulating elements and conventional, polarization-insensitive photodetectors. However, such extrinsic circular polarization selection often suffers from limited acceptance angle and technical difficulties in miniaturization and integration. Chiral organic semiconductors offer an appealing opportunity to directly integrate the CP selectivity into the photoactive layer of the device. They naturally come in pairs of structural mirror images known as enantiomers, which respond differently to CPL of opposite handedness.[3] This circular dichroism (CD) manifests in absorption only and should not be confused with circular Bragg reflection arising from mesoscopic structural ordering of, e.g., liquid crystals[4] and metamaterials.[5] Typically, for organic matter CD is a tiny optical effect. Although it has a paramount importance as spectroscopic tool,[6] it has essentially not been favored for technological applications in integrated photonic platforms so far.[7] Nevertheless, the combination of CD with semiconducting properties[8] enables optoelectronic detection[9,10] or emission[11,12] of CPL. For OLEDs, the CPL emission can be amplified by cholesteric organization of neat conjugated polymers[13] to enter the regime of technological relevance. However, organic photodiode detectors require a donor–acceptor blend to facilitate charge separation and cholesteric ordering would be disturbed by the commonly implemented bulk heterojunction (BHJ) concept.

Only very recently, we discovered that the CD response can be greatly enhanced by supramolecular aggregation in chiral squaraine thin films due to the nature of its excitonic coupling.[14] Importantly, the excitonic interactions are not

Dr. M. Schulz, Prof. A. Lützen
Kekulé Institute of Organic Chemistry and Biochemistry
University of Bonn
Bonn D-53121, Germany
Prof. F. Balzer
Mads Clausen Institute
University of Southern Denmark
Sønderborg DK-6400, Denmark
The ORCID identification number(s) for the author(s) of this article can be found under https://doi.org/10.1002/adfm.201900684.

DOI: 10.1002/adfm.201900684

Dr. D. Scheunemann, Prof. M. Schiek
Institute of Physics
University of Oldenburg
Oldenburg D-26129, Germany
E-mail: manuela.schiek@uni-oldenburg.de
Dr. O. Arteaga
Department of Applied Physics and IN2UB
University of Barcelona
Barcelona E-08028, Spain
Prof. S. C. J. Meskers
Department of Applied Physics
Eindhoven University of Technology
Eindhoven MB 5600, The Netherlands

disrupted in a BHJ blend allowing photovoltaic device operation under short circuit conditions without external power supply. For the present study, we implement enantiomerically pure prolinol-derived squaraines, (*R,R*)- and (*S,S*)-ProSQ-C6,[15] in conventional fullerene-blended BHJ photodiodes. The photodiodes directly convert CPL within the green spectral range into a handedness-dependent photocurrent under short circuit conditions, each enantiomer providing an opposite response. Moreover, the strong optical dissymmetry based on excitonic circular dichroism fully translates into a photocurrent dissymmetry for an intuitive device design. With that, we show that such photodiodes based on designed chiral organic semiconductors are able to efficiently differentiate between L- and R-CPL without the need for additional polarization manipulating optical elements. The self-powered photovoltaic operation combined with the mechanical flexibility and economic chemical tunability of soft matter in general invites smooth, sustainable, and biocompatible device design options.[16]

2. Results and Discussion

In **Figure 1**a, the structural formula of the chiral ProSQ-C6 is displayed. Both enantiomers have been obtained via a previously reported ex chiral pool strategy[15] with extended purification (see Note S1 in the Supporting Information). The ProSQ-C6 donor was blended with a conventional fullerene acceptor (PCBM) in a (2:3) mass ratio to act as photoactive layer in a conventional BHJ photodiode architecture as sketched in Figure 1b. The active layer has been subjected to thermal annealing at 60 °C and the thickness was varied throughout the experiments from 85 nm over 110 nm to 135 nm. Light entered the devices through a transparent indium tin oxide (ITO)-electrode modified with a thermally evaporated MoO_x hole transport layer. The cathode consisted of a reflecting aluminum layer directly evaporated onto the photoactive layer blend. We quantified the short circuit current I_{sc} for CPL illumination within the green spectral range (HeNe-laser at 543 nm) using alternating CPL illumination and lock-in detection (Figure 1b). Measurements have been performed without external voltage bias under self-powering photovoltaic short circuit conditions. The excitation wavelength has been chosen to match the spectral overlap of maximum absorbance (**Figure 2**a), maximum CD (Figure 2c,d), and maximum photocurrent response (**Figure 3**b,c). The current dissymmetry factor $g_{I_{sc}}$, i.e., the relative difference in I_{sc} upon alternating LCP and RCP illumination, has been calculated according to Equation (1) in the Experimental Section. The results for ProSQ-C6:PCBM devices with varying layer thicknesses are graphed in Figure 1c. The current dissymmetry amounted to $g_{I_{sc}} = 0.08 \pm 0.02$ for the (*R,R*)-devices, and to $g_{I_{sc}} = -0.10 \pm 0.01$ for the (*S,S*)-devices. The values were independent of layer thickness for the inspected range and have therefore been averaged over all measurements for the respective enantiomer. With that, the overall efficiency for the circular polarization discrimination amounted to about 5% with preferential sensitivity to LCP light for the (*R,R*)-enantiomer and preferential sensitivity to RCP light for the (*S,S*)-enantiomer.

To characterize the neat photoactive layer properties, we prepared thin films by spincoating on glass substrates with the same parameters as used for the devices. The absorbance spectra of such films were equivalent for the (*R,R*)- and the (*S,S*)-enantiomer (Figure 2a). For wavelengths shorter than 400 nm the absorbance stemmed from the PCBM and for wavelengths below 320 nm the glass substrate was opaque. The spectra were dominated by an intense absorption band within the green spectral range of visible light caused by the ProSQ-C6. The effective absorption coefficient of this maximum unpolarized absorbance at 545 nm extracted from ellipsometric data fitting amounted to approximately ≈177 000 cm^{-1}. Due to the chiral nature of the ProSQ-C6, the molecular aggregation caused a Davydov splitting of the absorbance spectrum.[17] The dominant spectral signature peaking at 545 nm can be understood as H-band (upper Davydov component) while the small peak at 750 nm represents a J-band (lower Davydov component). These features are blue-shifted (H-band) and red-shifted (J-band) compared to the monomer absorbance, which sharply peaks at 646 nm in chloroform solution.[15] However, no long range crystallographic order was detectable, as the samples were silent in X-ray diffraction experiments.[15] This was in line with microscopic inspection

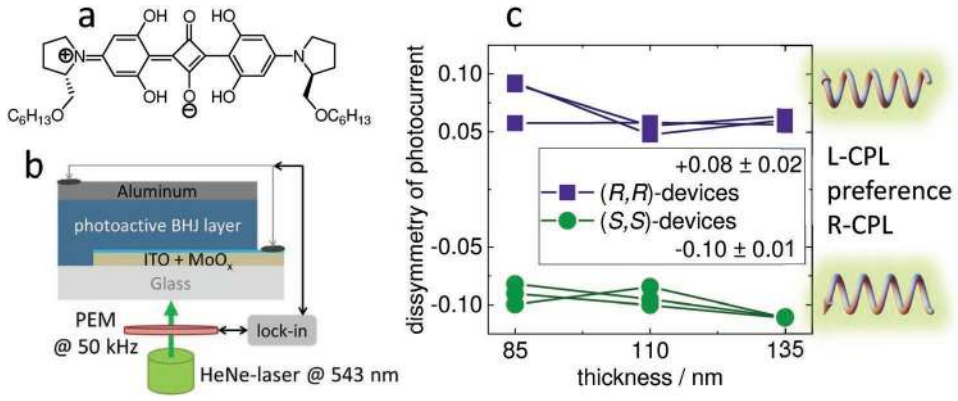

Figure 1. The circular polarized light detection performance: a) Structural formula of ProSQ-C6. b) Sketch of device architecture and setup for measuring the polarization resolved photocurrent response. c) Dissymmetry of short circuit current $g_{I_{sc}}$ under illumination with 543 nm CP light calculated according to Equation (1) for (*R,R*)- and (*S,S*)-ProSQ-C6:PCBM-blended devices with varying active layer thicknesses, lilac squares, and green circles, respectively. Lines are to guide the eye. The legend denotes the thickness averaged current dissymmetry.

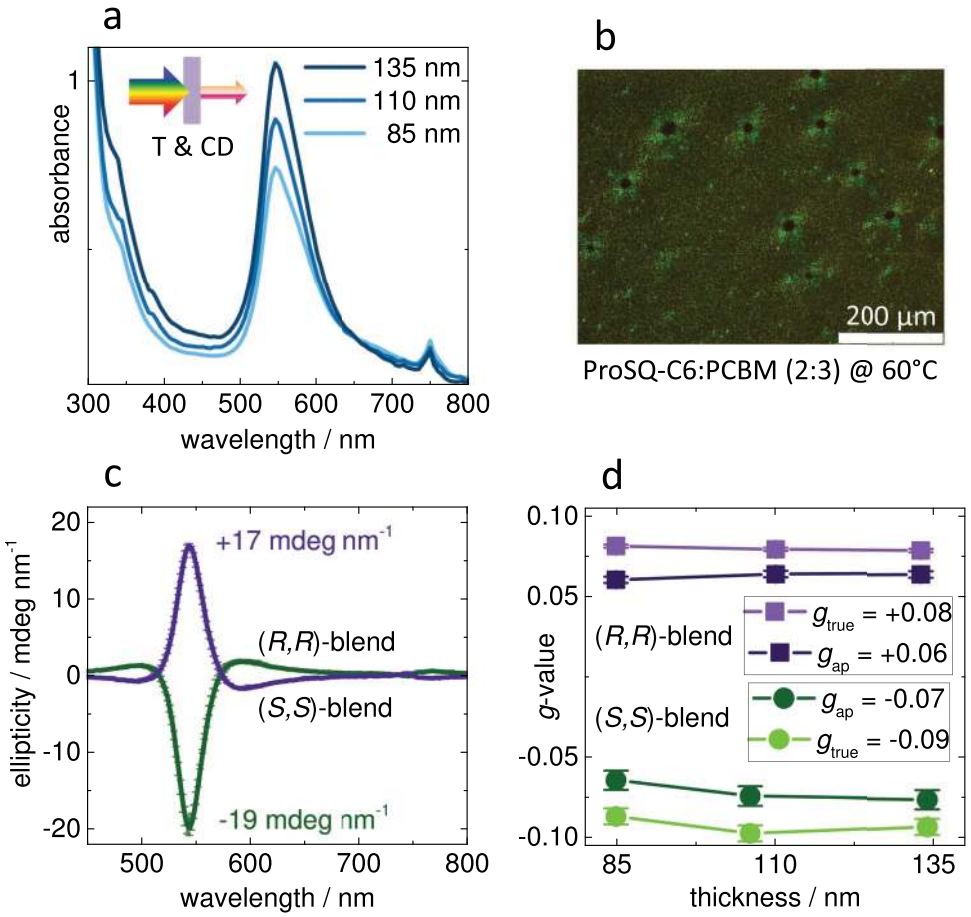

Figure 2. The circular dichroic photoactive layer blend: Analysis of (*R,R*)- and (*S,S*)-ProSQ-C6:PCBM-blended (2:3 mass ratio) thin films on glass annealed at 60 °C for three layer thicknesses (85, 110, and 135 nm): a) Global, unpolarized absorbance obtained from transmission measurements. The inset illustrates that CD manifests in transmission only. b) Overexposed microscopy image between crossed polarizers. c) Thickness normalized ellipticity averaged over the three layer thicknesses. Error bars are standard deviations. d) Maximum apparent and true dissymmetry factors, g_{ap} and g_{true}, at 545 nm according to Equations (5) and (6). Error bars are deduced from the experimental uncertainties. Lines are to guide the eye. The thickness averaged g_{ap} and g_{true} values are denoted in the legend.

between crossed-polarizers (Figure 2b), showing only a faint bireflectance circled around small irregularities within the otherwise featureless thin films.

We quantified the circular dichroic properties by Mueller matrix ellipsometry[14,18] of the active layer thin films. Complete exemplary differential Mueller matrices are plotted in Figures S2–S4 in the Supporting Information. In Figure 2c, the thickness normalized ellipticity according to Equation (2) in the Experimental Section is plotted for both enantiomers. The (*R,R*)-enantiomer showed a positive CD signal peaking at 545 nm indicating a preferred absorbance of L-CPL, while the response of the (*S,S*)-enantiomer was negative caused by preferential absorption of R-CPL. As expected, the ellipticity scaled linear with layer thickness. Thus, the thickness normalized measurements could reasonably be averaged to give about the same but opposite in sign values, (17 ± 0.3) and (–19 ± 1) mdeg nm^{-1} for the (*R,R*)- and (*S,S*)-enantiomer, respectively. This corresponded to a maximum differential extinction coefficient of $|\Delta k^{CP}| \approx 0.06$ at 545 nm calculated according to Equation (3) in the Experimental Section. The slightly inferior performance of the (*R,R*)-ProSQ-C6 most likely was due to a lower enantiomeric purity. Apparently, only the H-band spectral signature was CD-active while the J-band was CD-silent. The CD spectrum is conservative, meaning that the spectral integral over the CD signal including the wider side peaks approaches zero. This is indicative for an excitonic CD-response further supporting the idea of supramolecular aggregation within the thin films.[14] Most importantly, the excitonic coupling was not disrupted by intermixing with the fullerene acceptor. We could not detect circular Bragg reflection, underpinning that we report true circular dichroism which manifests in absorption only as illustrated by the inset in Figure 2a. In Figure 2d, the absorbance normalized apparent and true dissymmetry factors, g_{ap} and g_{true}, calculated at 545 nm are displayed for both enantiomers as a function of layer thickness. They have been determined according to Equations (4)–(6) in the Experimental Section. The true dissymmetry factor g_{true} accounts for reflection losses due to the thin film nature of the samples[14] (also see Figure S5 in the Supporting Information). As anticipated, the dissymmetry factor was an intensive quantity

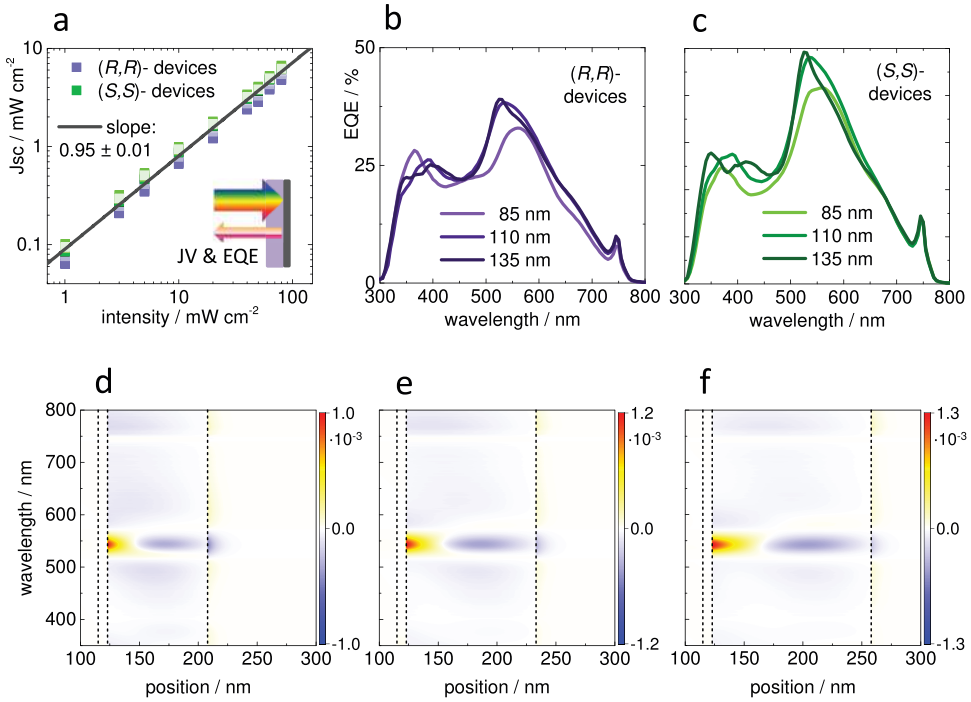

Figure 3. Photodiode device performance: a) Linear dynamic range (LDR) of all devices for unpolarized white light illumination. The inset illustrates the principle light path within the device for IV and EQE measurements. Note that CPL changes handedness upon reflection at a metallic interface such as the aluminum electrode. In (b) and (c), EQE spectra without background illumination under short circuit conditions of (*R,R*)- and (*S,S*)-ProSQ-C6:PCBM-blended devices, respectively, are displayed. In (d–f), 2D representations of the differential vertical absorption profiles within the devices of varying active layer thicknesses, 85, 110, and 135 nm, respectively, are shown. Dotted vertical lines in each plot indicate the following interfaces: at position 115 nm between ITO and MoO_x, at position 123 nm between MoO_x and active layer, and between active layer and aluminum electrode at positions 128 nm d), 238 nm e), and 258 nm f), respectively. Light enters the layer stack from the left side. The absorption profiles have been calculated according to Equation (8) using k^+ and k^-, Equation (7), simulating the response for the preferentially (+) and the nonpreferentially (−) absorbed CPL, respectively, valid for both the (*R,R*)- and the (*S,S*)-devices. The plots show the difference between preferred and nonpreferred absorption: $\Delta A^{CP}_{(x,\lambda)} = A^{+}_{(x,\lambda)} - A^{-}_{(x,\lambda)}$.

not depending on the layer thickness. The magnitudes of the thickness-averaged apparent dissymmetry factors amounted to 0.06 ± 0.002 and −0.07 ± 0.006 for the (*R,R*)- and (*S,S*)-enantiomer, respectively. The values increased slightly upon reflection correction resulting in g_{true} = 0.08 ± 0.001 and g_{true} = −0.09 ± 0.005 for the (*R,R*)- and (*S,S*)-enantiomer, respectively. Standard deviations for the thickness-averaging are stated. Most essential here, the corrected optical dissymmetry data were on the same order and showed the same CPL preference as the photocurrent dissymmetry displayed in Figure 1c. In case of the devices, the light passes the active layer twice as illustrated in the inset of Figure 3a, which is different compared to the transmission measurements on the photoactive layer alone (inset in Figure 2a). In view of the fact that CPL reverses its handedness upon reflection at metallic interfaces just as the aluminum backelectrode, we need to understand the device performance better.

Current density–voltage (*JV*) curves have been recorded under unpolarized, simulated sun light with variable irradiance ranging from 100 to 1 mW cm^{-2}. Complete exemplary sets of *JV* curves for both enantiomers with three layer thicknesses (85, 110, and 135 nm) are plotted in Figure S6 in the Supporting Information. The averaged key photovoltaic performance parameters for full illumination are summarized in Table S1 in the Supporting Information. The device performance was only slightly affected by the layer thickness consequently resulting in a very similar power conversion efficiency of around 2.5% for all devices. The fill factor was with around 56% remarkably good for solution-processed squaraine-based photodiodes.[19] The short circuit current density (J_{sc}) as function of illumination intensity is plotted in Figure 3a for all inspected devices. For 1 sun illumination J_{sc} equals ≈6.5 mA cm^{-2}. We found basically a linear scaling of J_{sc} for the chosen illumination intensity range. This means that the linear dynamic range (LDR) of the devices spanned at least two orders of magnitude, i.e., LDR ≥ 4 dB. With that, we could greatly improve the performance compared to our previous paper reporting a power conversion efficiency below 1.0%, a fill factor of only 36%, and a space-charge-limitation for higher illumination intensities.[15] This was due to the extended purification procedure of the ProSQ-C6 compounds and, more pronounced, to the omission of a LiF interlayer at the aluminum cathode. Such thin LiF interlayers are widely used to enhance charge injection/extraction in organic electronic devices.[20] However, in our case of the ProSQ-C6 material, charge extraction was impaired. Furthermore, we had noticed rapid degradation even for storage in inert atmosphere for LiF containing devices.

The external quantum efficiency (EQE) shows the spectrally resolved photocurrent and is plotted for the (*R,R*)-enantiomer in Figure 3b and for the (*S,S*)-enantiomer in Figure 3c.

The spectra have been recorded without any background illumination under short circuit conditions. The EQE for the (*S,S*)-enantiomer was slightly higher compared to the (*R,R*)-enantiomer, which was in analogy to the quantification of the CD-response of the respective photoactive layer blend. We consider this as a matter of a higher impurity level for the (*R,R*)-enantiomer. Otherwise, the EQE spectra looked as expected very similar for both enantiomers. Furthermore, the spectral course did not change much with varying layer thickness allowing for a resilient device design. Most importantly, we can see that the H-band spectral signature within the green gave the strongest photocurrent response, which was up to 40% for the (*R,R*)-enantiomer and up to 50% for the (*S,S*)-enantiomer. Thus, there was a good spectral overlap of maximum CD-response and photocurrent-response.

In the following, we rationalize that the optical dissymmetry fully translated into a photocurrent dissymmetry. For this we proof that the main photocurrent generation from green light happens before the light is backreflected at the cathode and, therefore, is not affected by thin film interference. If backreflected, handedness-reversed light would contribute to photocurrent generation within the CD-active spectral range, the polarization-selective response would be compensated or reversed.[9] Similar modeling approaches have also been undertaken for, e.g., CPL OLEDs.[11] For this we calculated 2D absorption profiles $A^{\pm}_{(x,\lambda)}$ of the devices for unpolarized illumination via transfer matrix optical calculations[21] according to Equation (8) in the Experimental Section.[22] Calculations have been performed using modified extinction coefficients k^+ and k^-, respectively, obtained from the effective, isotropic extinction coefficient, k_{eff}, plus/minus half the differential extinction coefficient $|\Delta k^{\text{CP}}|$, Equation (7) in the Experimental Section and Figure S7 in the Supporting Information . With that a response to preferentially (+) and nonpreferentially (–) absorbed CPL, $A^{+}_{(x,\lambda)}$ and $A^{-}_{(x,\lambda)}$, respectively, could be simulated. This means that $A^{+}_{(x,\lambda)}$ ($A^{-}_{(x,\lambda)}$) corresponds to the response of the (*R,R*)-devices to L-CPL (R-CPL) and vice versa. In Figure 3d–f, the differential 2D absorption profiles $\Delta A^{\text{CP}}_{(x,\lambda)} = A^{+}_{(x,\lambda)} - A^{-}_{(x,\lambda)}$ valid for both (*R,R*)- and (*S,S*)-devices are plotted for the three investigated layer thicknesses (85, 110, and 135 nm). The complete absorption profiles $A^{+}_{(x,\lambda)}$ and $A^{-}_{(x,\lambda)}$ are displayed in Figure S8 in the Supporting Information. In all three cases, green light is almost fully absorbed close to the anode due to the large overall absorption coefficient of the ProSQ-C6. Thus charge carriers relevant for the CPL discriminating photocurrent can efficiently be extracted. The differential absorption profiles show that the absorption of the nonpreferred CPL around 545 nm extends a bit further into the active layer very similar for all three layer thicknesses. To proof that this behavior is not a result of interference effects caused by the reflecting aluminum electrode, we calculated semi-infinite active layer devices by replacing the aluminum with a ProSQ-C6:PCBM layer within the stack. The complete absorption profiles $A^{+}_{(x,\lambda)}$ and $A^{-}_{(x,\lambda)}$ together with the differential absorption $\Delta A^{\text{CP}}_{(x,\lambda)}$ for the semi-infinite devices are displayed in Figure S9 in the Supporting Information. Indeed, the full absorption profiles of real devices are dominated by interference patterns while the infinite active layer devices are not. However, the differential absorption profiles for the CD-active spectral range around 545 nm are essentially the same in both cases. Thereby we demonstrate, that 1) the single light path is sufficient to absorb all light within the green CD-active spectral range, and 2) that the optical dissymmetry translates into a spatial charge carrier generation profile located close to the anode, and 3) that this profile is insensitive to active layer thickness variation. Squaraines in general are low-mobility donor materials potentially causing photodiodes to suffer from extraction losses.[19] Therefore, the spatial generation profile directly connects to a preferred charge extraction profile giving the photocurrent output. Thus, preferential absorbed CPL, L-CPL for the (*R,R*)-enantiomer, and R-CPL for the (*S,S*)-enantiomer, translated into a photocurrent of the devices that was higher by the same extend as the optical dissymmetry. In other words g_{true} equaled $g_{I_{\text{sc}}}$ roughly being ±0.1, resulting in 5% overall CP discrimination efficiency.

This is approximately a tenfold increase in CP discrimination efficiency compared to the previously reported polymer-based bilayer devices.[9] Furthermore, the bilayer devices suffered from a strongly thickness dependent g_{ap} and a counter-intuitive polarization sensitivity, i.e., the current dissymmetry was of opposite sign compared to the optical dissymmetry of neat polymer layers. These polymer layers had a substantially smaller (differential) absorption coefficient because they neither showed supramolecular excitonic interactions nor cholesteric ordering. The latter, mesoscopic structural ordering, would be impaired by intermixing with a fullerene acceptor. Therefore, introducing supramolecular aggregation, that could be conserved in a donor–acceptor blend, is the preferred route to a sizable excitonic CD response. With the design of the prolinol-derived squaraines, we have successfully installed excitonic CD combined with semiconducting properties well suited for photodiode device performance. In case of the present ProSQ-C6:PCBM photodiodes, the devices scored with ease of preparation due to the BHJ-architecture, and with a straightforward polarization sensitivity without optical interference losses due to the high (circular dichroic) extinction based on excitonic coupling.

3. Conclusion

In conclusion, we have successfully prepared organic photodiode CPL sensors based on circular dichroic squaraine:fullerene BHJ photoactive layer blends. The targeted high absorption coefficient and the strong excitonic circular dichroism originating from supramolecular aggregation are not disrupted by intermixing of the fullerene acceptor. The prolinol-derived squaraine enantiomers of opposite handedness showed reverse differential photocurrent responses of equal magnitude under short circuit conditions. Thereby, they are able to discriminate between L- and R-CPL light within the green spectral range without the need for additional polarization manipulating optical elements and external power supply. The excitonic optical dissymmetry translated fully into a photocurrent dissymmetry, because of a single optical path spatial charge carrier generation profile confined close to the anode within the CD active spectral range. Altogether, this allows a straightforward, robust device design, and ease of preparation and handling to match the demands of future sustainable and wearable consumer electronics.

With a photocurrent dissymmetry factor up to $g_{I_{sc}} = \pm 0.1$ corresponding to 5% overall efficiency for the polarization discrimination, chiral excitonic soft matter advances a regime of technological relevance. This is a leap forward toward the future development of flexible and compact integrated platforms for chiroptical imaging and sensing units.

4. Experimental Section

Synthesis: The (*R,R*)- and (*S,S*)-ProSQ-C6 were obtained via a chiral pool strategy similar to the previously published route[15] adopted from literature.[23] Details on the synthesis and full analytical details can be found in Note S1 in the Supporting Information.

Thin Film and Device Preparation: All bulk heterojunction photoactive layers were obtained by spincoating from a 15 mg mL^{-1} solution of ProSQ-C6 and phenyl-C61-butyric acid methyl ester (PCBM; Solenne BV) with 2:3 mass fraction in amylene-stabilized chloroform (Sigma-Aldrich). For Mueller matrix ellipsometry and general ellipsometry objective, slides from VWR cut into $(15\ mm)^2$ pieces served as substrates. For photodiode devices, the photoactive layers were sandwiched between an ITO (Temicon) anode coated with 8 nm substoichiometric molybdenum oxide MoO_x by thermal vapor deposition of molybdenum(VI)oxide (Sigma-Aldrich) and an evaporated aluminum electrode (250 nm) (also see Figure 1b and Table S1 in the Supporting Information). Active device areas were around 0.1 cm^2. All preparation was done in a nitrogen filled glove box.

Polarization Resolved Short Circuit Current: The short circuit currents of the photodiodes ${}^{L}I_{sc}$ and ${}^{R}I_{sc}$ upon illumination with left (L) and right (R) circularly polarized light, respectively were determined as follows (also see Figure 3a). Linearly polarized green light (543 nm) from a HeNe laser (2 mW, beam diameter 3 mm) was passed through a photoelastic modulator (PEM). This resulted in a beam of constant light intensity but with alternating circular polarization between L and R with a modulation period (frequency) of 20 µs (50 kHz). By using a lock-in amplifier (Stanford Research SR830), the differential short circuit current ${}^{L}I_{sc} - {}^{R}I_{sc}$ was directly determined. This method works well for currents within the nanoampere range. Inserting a left (right) circular polarizer in the optical path before the PEM allowed for estimation of the absolute current ${}^{L}I_{sc}$ (${}^{R}I_{sc}$). Here, the value was corrected for the optical density of the filter assuming a linear scaling of the current with light intensity. The relative difference in I_{sc} upon L and R polarized illumination, the dissymmetry factor $g_{I_{sc}}$, was then calculated according to

$$g_{I_{sc}} = \frac{{}^{L}I_{sc} - {}^{R}I_{sc}}{0.5 \cdot ({}^{L}I_{sc} + {}^{R}I_{sc})} \tag{1}$$

Mueller Matrix Ellipsometry and Circular Dichroic Properties: A Woollam variable angle spectroscopic ellipsometer (VASE) with a polarizer-compensator-sample-analyzer (PCSA) configuration with the monochromator entrance slit narrowed to 600 µm to reach a 2 nm spectral resolution was used to record 11, i.e., the first three rows, out of the 15 normalized elements of the (4 × 4) Mueller matrix **M**. The differential Mueller matrix **L** was calculated after adding the missing matrix row by symmetry considerations for sufficiently nondepolarizing samples[24] to extract the circular dichroism CD as the average of the matrix elements l_{03} and l_{30} (see ref. [14] for details). The differential Mueller matrices can be found in Figures S2–S4 in the Supporting Information. Here, the ellipticity can be correctly obtained by the small value approximation

$$\theta = \mathrm{CD}/2 \tag{2}$$

Both CD and θ scale linear with optical pathlength and can reasonably be normalized to the layer thickness d, which here was obtained by conventional ellipsometry scans fitted with a Cauchy layer within the transparent spectral regime.

From CD, the differential imaginary part of the refractive index Δk^{CP} (differential extinction coefficient) for L-CPL and R-CPL can be calculated according to

$$\Delta k^{CP} = k^{L} - k^{R} = \frac{\mathrm{CD}}{d} \cdot \frac{\lambda}{2\pi} \tag{3}$$

The differential circular absorbance of L-CPL and R-CPL is calculated by

$$\Delta \mathrm{Abs}^{CP} = \mathrm{Abs}^{L} - \mathrm{Abs}^{R} = \frac{2 \cdot \mathrm{CD}}{\ln(10)} \tag{4}$$

The absorbance normalized apparent dissymmetry factor g_{ap} is obtained by

$$g_{ap} = \frac{\Delta \mathrm{Abs}^{CP}}{\mathrm{Abs}^{meas}} \tag{5}$$

with $\mathrm{Abs}^{meas} = -\log(T)$ being the measured unpolarized absorbance of the sample. Transmission data were measured with linear polarized light under normal incidence. Here, the global absorbance was essentially the same for polarized and unpolarized light, as expected for sufficiently nondepolarizing samples. The apparent dissymmetry factor contained interfacial reflection losses due to the thin film nature of the samples.[14] These reflection losses were accounted for to obtain the true dissymmetry factor g_{true}

$$g_{true} = \frac{\Delta \mathrm{Abs}^{CP}}{\mathrm{Abs}^{cor}} \tag{6}$$

where Abs^{cor} is the reflection-corrected absorbance (Figure S5, Supporting Information), as introduced previously.[14]

Unpolarized JV and EQE Measurements: Current–voltage characteristics were measured with a Keithley 4200 semiconductor characterization system with four-probe sensing under a Photo Emission Tech. AAA solar simulator providing an AM1.5G spectrum. The intensity was adjusted to 100 mW cm^{-2} with a calibrated Si solar cell for full illumination. A set of neutral density filters was used to vary the irradiance. Photovoltaic performance parameter can be found in Table S1 in the Supporting Information and intensity dependent *JV* curves in Figure S6 in the Supporting Information.

A Bentham PVE300 system equipped with a dual Xenon/quartz halogen light source, a Czerny-Turner TMc300 monochromator, and an integrating sphere was used to record the external quantum efficiency. The quadratic spot size of the monochromatic light beam was set to $(0.74\ mm)^2$. The monochromator entrance slit was set to 1.85 mm offering 5 nm spectral resolution for the monochromatic light beam, which was modulated at ≈660 Hz by a chopper wheel. The spectra were referenced to the EQE of a calibrated Si solar cell. The photocurrent was recorded using a Stanford Research SR830 lock-in amplifier after passing a transimpedance amplifier.

Optical Constants and Transfer Matrix Optical Calculations: The effective optical constants n and k_{eff} of the active layer blend were determined from fitting spectroscopic ellipsometry data acquired with a Woollam VASE as detailed out in Note S2 in the Supporting Information.

Calculations were performed using modified extinction coefficients simulating the response to preferentially and nonpreferentially absorbed CPL, k^{+} and k^{-}, respectively

$$k^{\pm} = k_{eff} \pm 0.5 \cdot |\Delta k^{CP}| \tag{7}$$

with Δk^{CP} being the differential absorption coefficient according to Equation (3).

The corresponding preferential and nonpreferential absorption, $A^{+}_{(x,\lambda)}$ and $A^{-}_{(x,\lambda)}$, as a function of wavelength λ within the photoactive layer at the position x of a device was calculated according to[22]

$$A^{\pm}_{(x,\lambda)} = n_{(\lambda)} \cdot \frac{4\pi}{\lambda} \cdot k^{\pm}_{(\lambda)} \cdot |E^{\pm}_{(x,\lambda)}|^2 \quad (8)$$

The distribution of the electrical field intensity $|E^{\pm}_{(x,\lambda)}|^2$ was obtained by the transfer matrix method for optically multilayer systems with coherent and incoherent interfaces using a customized, readily available MATLAB script.[21]

Supporting Information

Supporting Information is available from the Wiley Online Library or from the author.

Acknowledgements

M.S., M.S., and D.S. thank Prof. J. Parisi (head of Energy and Semiconductor Laboratory Division, University of Oldenburg) most sincerely for his shared-labs policy thereby providing access to a variety of state-of-the-art equipment including technical support. For the latter, the authors are indebted to Matthias Macke, Ulf Mikolajczak, and Janet Neerken.

Conflict of Interest

The authors declare no conflict of interest.

Keywords

chiral organic semiconductors, circular polarized light, excitonic circular dichroism, Mueller matrix ellipsometry, photovoltaic photodetectors

Received: January 21, 2019
Revised: February 10, 2019
Published online: March 6, 2019

[1] B. Y. Toh, R. Cahill, V. Fusco, *IEEE Trans. Educ.* **2003**, *46*, 313.
[2] J. Geng, *Adv. Opt. Photonics* **2013**, *5*, 456.
[3] a) J. R. Brandt, F. Salerno, M. J. Fuchter, *Nat. Rev. Chem.* **2017**, *1*, 1; b) K. Michaeli, N. Kantor-Uriel, R. Naaman, D. H. Waldeck, *Chem. Soc. Rev.* **2016**, *45*, 6478.
[4] a) G. Lakhwani, S. C. J. Meskers, *J. Phys. Chem. A* **2011**, *116*, 1121; b) J. Kobashi, H. Yoshida, M. Ozaki, *Nat. Photonics* **2016**, *10*, 389.
[5] E. Plum, X.-X. Liu, V. A. Fedotov, Y. Chen, D. P. Tsai, N. I. Zheludev, *Phys. Rev. Lett.* **2009**, *102*, 113902.
[6] N. Berova, P. L. Polavarapu, K. Nakanishi, R. W. Woody, *Comprehensive Chiroptical Spectroscopy, 2 Volume Set*, John Wiley & Sons, NY **2014**.
[7] W. Li, Z. J. Coppens, L. V. Besteiro, W. Wang, A. O. Govorov, J. Valentine, *Nat. Commun.* **2015**, *6*, 8379.
[8] Y. Yang, B. Rice, X. Shi, J. R. Brandt, R. C. da Costa, G. J. Hedley, D.-M. Smilgies, J. M. Frost, I. D. W. Samuel, A. O. de-la Roza, E. R. Johnson, K. E. Jelfs, J. Nelson, A. J. Campbell, M. J. Fuchter, *ACS Nano* **2017**, *11*, 8329.
[9] J. Gilot, R. Abbel, G. Lakhwani, E. W. Meijer, A. P. H. J. Schenning, S. C. J. Meskers, *Adv. Mater.* **2010**, *22*, E131.
[10] a) Y. Yang, R. C. da Costa, M. J. Fuchter, A. J. Campbell, *Nat. Photonics* **2013**, *7*, 634; b) X. Shang, I. Song, H. Ohtsu, Y. H. Lee, T. Zhao, T. Kojima, J. H. Jung, M. Kawano, J. H. Oh, *Adv. Mater.* **2017**, *29*, 1605828; c) G. Albano, F. Salerno, L. Portus, W. Porzio, L. A. Aronica, L. Di Bari, *ChemNanoMat* **2018**, *4*, 1059; d) J. Yoshida, S. Tamura, H. Yuge, G. Watanabe, *Soft Matter* **2018**, *14*, 27; e) N. Y. Kim, J. Kyhm, H. Han, S. J. Kim, J. Ahn, D. K. Hwang, H. W. Jang, B.-K. Ju, J. A. Lim, *Adv. Funct. Mater.* **2019**, 1808668, https://doi.org/10.1002/adfm.201808668.
[11] F. Zinna, M. Pasini, F. Galeotti, C. Botta, L. D. Bari, U. Giovanella, *Adv. Funct. Mater.* **2016**, *27*, 1603719.
[12] a) D. Di Nuzzo, C. Kulkarni, B. Zhao, E. Smolinsky, F. Tassinari, S. C. Meskers, R. Naaman, E. Meijer, R. H. Friend, *ACS Nano* **2017**, *11*, 12713; b) F. Zinna, U. Giovanella, L. D. Bari, *Adv. Mater.* **2015**, *27*, 1791; c) J. R. Brandt, X. Wang, Y. Yang, A. J. Campbell, M. J. Fuchter, *J. Am. Chem. Soc.* **2016**, *138*, 9743; d) F. Song, Z. Xu, Q. Zhang, Z. Zhao, H. Zhang, W. Zhao, Z. Qiu, C. Qi, H. Zhang, H. H. Y. Sung, I. D. Williams, J. W. Y. Lam, Z. Zhao, A. Qin, D. Ma, B. Z. Tang, *Adv. Funct. Mater.* **2018**, *28*, 1800051; e) M. Li, S.-H. Li, D. Zhang, M. Cai, L. Duan, M.-K. Fung, C.-F. Chen, *Angew. Chem., Int. Ed.* **2018**, *57*, 2889; f) J. Han, S. Guo, H. Lu, S. Liu, Q. Zhao, W. Huang, *Adv. Opt. Mater.* **2018**, *6*, 1800538.
[13] C. Kulkarni, S. C. J. Meskers, A. R. A. Palmans, E. W. Meijer, *Macromolecules* **2018**, *51*, 5883.
[14] M. Schulz, J. Zablocki, O. S. Abdullaeva, S. Brück, F. Balzer, A. Lützen, O. Arteaga, M. Schiek, *Nat. Commun.* **2018**, *9*, 2413.
[15] M. Schulz, M. Mack, O. Kolloge, A. Lützen, M. Schiek, *Phys. Chem. Chem. Phys.* **2017**, *19*, 6996.
[16] a) J. Clark, G. Lanzani, *Nat. Photonics* **2010**, *4*, 438; b) O. S. Abdullaeva, F. Balzer, M. Schulz, J. Parisi, A. Lützen, K. Dedek, M. Schiek, *Adv. Funct. Mater.* **2019**, https://doi.org/10.1002/adfm.201805177.
[17] a) N. J. Hestand, F. C. Spano, *Chem. Rev.* **2018**, *118*, 7069; b) K. A. Kistler, C. M. Pochas, H. Yamagata, S. Matsika, F. C. Spano, *J. Phys. Chem. B* **2011**, *116*, 77.
[18] a) J. J. G. Pérez, R. Ossikovski, *Polarized Light and the Mueller Matrix Approach*, CRC Press, Boca Raton, FL **2016**; b) A. Mendoza-Galván, E. Muñoz-Pineda, S. J. Ribeiro, M. V. Santos, K. Järrendahl, H. Arwin, *J. Opt.* **2018**, *20*, 024001.
[19] a) D. Scheunemann, O. Kolloge, S. Wilken, M. Mack, J. Parisi, M. Schulz, A. Lützen, M. Schiek, *Appl. Phys. Lett.* **2017**, *111*, 183502; b) S. Brück, C. Krause, R. Turrisi, L. Beverina, S. Wilken, W. Saak, A. Lützen, H. Borchert, M. Schiek, J. Parisi, *Phys. Chem. Chem. Phys.* **2014**, *16*, 1067; c) G. Chen, H. Sasabe, T. Igarashi, Z. Hong, J. Kido, *J. Mater. Chem. A* **2015**, *3*, 14517.
[20] S. Torabi, J. Liu, P. Gordiichuk, A. Herrmann, L. Qiu, F. Jahani, J. C. Hummelen, L. J. A. Koster, *ACS Appl. Mater. Interfaces* **2016**, *8*, 22623.
[21] G. F. Burkhard, E. T. Hoke, M. D. McGehee, *Adv. Mater.* **2010**, *22*, 3293.
[22] D. Scheunemann, S. Wilken, J. Parisi, H. Borchert, *ACS Photonics* **2015**, *2*, 864.
[23] R. S. Stoll, N. Severin, J. P. Rabe, S. Hecht, *Adv. Mater.* **2006**, *18*, 1271.
[24] a) O. Arteaga, *Opt. Lett.* **2013**, *38*, 1131; b) O. Arteaga, B. Kahr, *Opt. Lett.* **2013**, *38*, 1134.